Progress In Electromagnetics Research, Vol. 130, 187–206, 2012

INVESTIGATION OF FANO RESONANCES INDUCED BY HIGHER ORDER PLASMON MODES ON A CIRCULAR NANO-DISK WITH AN ELONGATED CAVITY

M. Amin and H. Bağcı*

Division of Physical Sciences and Engineering, King Abdullah, University of Science and Technology (KAUST), Thuwal 23955-6900, Saudi Arabia

Abstract—In this paper, a planar metallic nanostructure design, which supports two distinct Fano resonances in its extinction cross-section spectrum under normally incident and linearly polarized electromagnetic field, is proposed. The proposed design involves a circular disk embedding an elongated cavity; shifting and rotating the cavity break the symmetry of the structure with respect to the incident field and induce higher order plasmon modes. As a result, Fano resonances are generated in the visible spectrum due to the destructive interference between the sub-radiant higher order modes and super-radiant the dipolar mode. The Fano resonances can be tuned by varying the cavity's width and the rotation angle. An RLC circuit, which is mathematically equivalent to a mass-spring oscillator, is proposed to model the optical response of the nanostructure design.

1. INTRODUCTION

It is well known that nanostructures constructed using metallic particles are capable of supporting surface plasmon modes with resonance frequencies in the visible spectrum [1, 2]. These modes are simply collective oscillations of conduction electrons excited by a high frequency electromagnetic wave (i.e., light) incident on the structure. When the structure is electrically small, i.e., its largest dimension is sub-wavelength, the optical properties of these plasmon modes depend almost exclusively on the specific shape of the structure [3]. This allows for easy tuning of the plasmon modes' resonance frequency, localized field amplitudes, quality factor, and line-width via only simple

Received 5 April 2012, Accepted 31 May 2012, Scheduled 10 August 2012

* Corresponding author: Hakan Bağcı (hakan.bagci@kaust.edu.sa).

modifications of the structure's geometric parameters. This highly desired easy tuning property has led to the development of many plasmonic structures constructed using spheres [4, 5], ellipsoids [6], eggs [7], shells [8], and circular disks [9] and rings [10] for various applications in bio- and chemical sensing [11–14], designing plasmonic light sources, and waveguides, metamaterial absorbers [15, 16], multiresonance filters [17], and materials with effective negative index [18–21]. For bio- and chemical sensing applications, open quasi three-dimensional (disk and ring-like) structures are preferred over their closed counterparts because of their capacity to contain greater volumes of molecules in the vicinity of structure within the near field of the plasmon modes [22].

Recently, generation of Fano resonances on nanostructures via interference of plasmon modes, an effect similar to electromagnetic induced transparency in atomic systems [23, 24], has become a topic of interest due to its promising applications in light manipulation [25], bio- and chemical sensing, and optical switching [26, 27]. Plasmonic Fano resonances are obtained from the coherent interference between super- and sub-radiant plasmon modes; this can be achieved using either (anti-parallel) dipolar modes [28, 29] or a dipolar and a higher order mode (i.e., quadrapolar, octopolar modes) [30–34]. When the structure is electrically small and symmetric with respect to incident field's polarization and/or direction of propagation, higher order modes cannot be excited by the incident field [35–38]. One can increase the electrical size of structure (at the cost of ease of tunability) [10] or 'break' the structural symmetry [35] to permit the incident field's energy to couple to the dark higher order modes. Symmetry breaking has been proven useful in excitation of higher order modes to generate plasmonic Fano resonances for various nanostructures constructed from shells [28, 32, 35], disks [9, 36] and rings [34, 37, 38] as well as in design of resonators used for construction of metamaterials at lower frequencies [39]. Other examples of symmetry breaking methods include using conductive coupling between a theta-shaped ring rod and the wall of the ring enclosing it [40] and removing a wedge slice from a metallic nanodisk [41]. It is well known that any physical Fano resonance can be mathematically modeled using a multi-resonance coupled system of oscillator equations [35]. To this end, the mass spring model has been accurately applied in explanation of one or two Fano resonances observed in the extinction cross-section (CS) spectrum of various nano-scale devices [35, 42–44, 53].

In this work, the presence of two distinct Fano resonances in the optical response of a sub-wavelength planar metallic nanostructure to normally incident and linearly polarized electromagnetic field is

demonstrated. The nanostructure is constructed from a circular gold disk embedding an elongated cavity. Top view of the structure and description of the incident electromagnetic field are given in Fig. 1(a). The higher order modes, which provide the mechanism for Fano resonance generation, are obtained via symmetry breaking. This is implemented by combining two approaches: (i) The elongated cavity is shifted along the horizontal axis of the disk [Fig. 1(b)] and (ii) it is rotated around the normal of the disk [Fig. 1(c)]. Numerical simulations have demonstrated the presence of three distinct plasmon resonances in the extinction CS spectrum of this anti-symmetric geometry. Spectral tuning of these plasmonic resonances through modification of the geometry parameters produces two distinct Fano resonances in the visible spectrum. These results suggest that the disk with the shifted and rotated elongated cavity can be used as the building block of devices for generating slow light in bio- and chemical

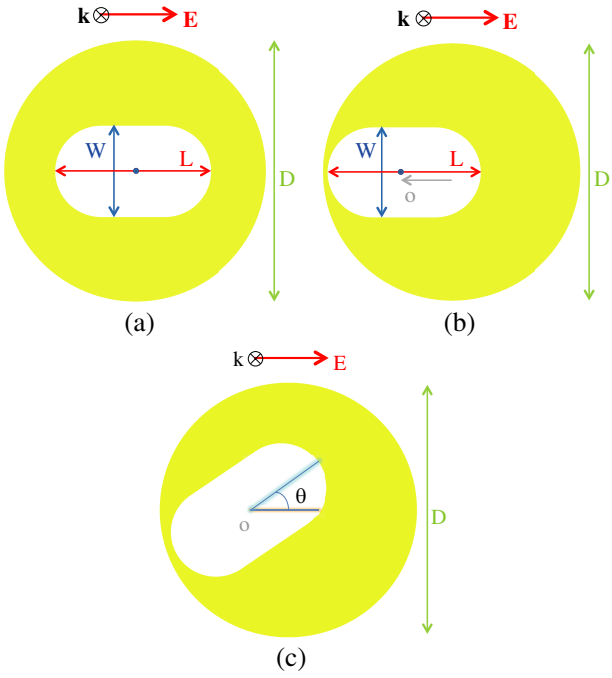

Figure 1. Description of the incident electromagnetic field and the top views of the the circular disk with (a) the concentric elongated cavity, (b) the shifted elongated cavity, and (c) the shifted and rotated elongated cavity.

sensing applications. Additionally, in this work, the optical response of the proposed design is compared to the response of an RLC circuit, which is mathematically equivalent to that of a mass-spring oscillator.

It should be emphasized here the design of the circular gold disk embedding a shifted and rotated elongated cavity is distinguished from previously developed ring-like structures by two novel characteristics: (i) Two distinct Fano resonances are generated in the extinction CS spectrum and this is achieved using only one layer of metal without the need for a metallic multi-layered shell. (ii) Elongated cavity is not cylindrically symmetric. This introduces the rotation angle of the cavity as another tuning variable and provides more flexibility for applications requiring operation in different frequency bands.

The remainder of the paper is organized as follows. In Section 2.1, an initial design with a concentric elongated cavity is introduced and it is shown that this design supports a super-radiant dipolar mode in the visible spectrum under a normally incident x-polarized plane wave. Note that the elongated cavity's major axis is along the x-axis. In Section 2.2, it is shown that breaking the symmetry of the initial design with respect to the excitation by shifting the cavity along the x-axis permits higher order plasmon modes in the visible spectrum. The interference between the dipolar mode and the quadrupolar mode generates a Fano resonance dip in the spectrum. Additionally, tunability of the Fano resonace is also demonstrated: Decreasing the width of the cavity moves the locations of the dipolar and quadrupolar modes closer and improves the line shape of the Fano resonance. In Section 2.3, it is shown that the structural asymmetry introduced by rotating the shifted elongated cavity around the normal of the disk introduces another dipolar mode in the visible spectrum generating an additional Fano resonance dip. These Fano resonances can be tuned by modifying cavity's rotation angle. In Section 3, it is shown that the total power drawn by an RLC circuit can be used to mathematically model the extinction CS of the proposed designs. Section 5 summarizes the contribution of the work and draws future research directions.

2. DESIGN AND TUNABILITY

2.1. Disk with Concentric Elongated Cavity

To demonstrate the presence of a super-radiant dipolar plasmonic mode in the visible spectrum, an initial design consisting of a gold disk and a concentric embedded elongated cavity is considered first [Fig. 1(a)]. The diameter and height of the disk and the length and width of the elongated cavity are $D = 100\,\text{nm}$ and $H = 10\,\text{nm}$

and $L = 65.5\,\text{nm}$ and $W = 35\,\text{nm}$, respectively. These specific dimensions allow generation of dipolar and quadrupolar modes (which destructively interfere to induce Fano resonances) within the visible part of the spectrum. It should be mentioned here that as long as the overall size of the disk is a fraction of the wavelength, scaling the geometric parameters of the design (i.e., keeping their ratio the same) does not significantly change the response of the system (for example see [51, 52] for a detailed discussion on the effect of scaling on the optical response of a hole in a metal film). In this work, D, L, and W are large enough to allow for generation of higher-order modes and also small enough to avoid large phase retardation effects, which is well-known to complicate the design of the structure. The structure is excited with a normally incident x-polarized plane wave. Due to the symmetry of the structure with respect to the excitation, only a dipolar mode is excited; higher order modes remain dark. This is clearly demonstrated by the extinction CS spectrum presented in Fig. 2. This dipolar mode is named D_1 in the remainder of the text. As shown by the surface charge distribution on the structure around D_1's resonance frequency (inset of Fig. 2), D_1 possesses a non-zero dipole moment along the x-axis. Therefore the corresponding resonance in the extinction CS spectrum becomes visible under the excitation with an x-polarized incident field. However, higher order modes remain dark since they do not possess the dipole moment that would permit the incident field's energy to couple to the modes.

It should be noted here that the plasmon hybridization theory [45]

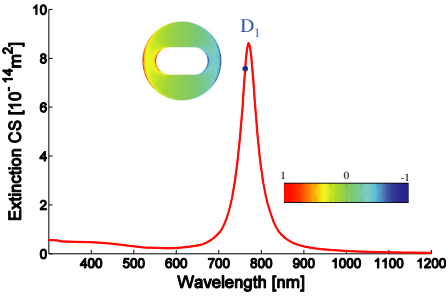

Figure 2. Extinction CS spectrum of the circular disk with the concentric elongated cavity. The geometry parameters shown in Fig. 1(a) and the height of the structure are $D = 100\,\text{nm}$, $L = 65.5\,\text{nm}$, $W = 35\,\text{nm}$, and $H = 10\,\text{nm}$ respectively. The inset shows the charge distribution on the structure at 762 nm, marked with the blue dot on the plot. The charge distribution shown in the color plot is normalized between -1 (blue) and 1 (red).

can be used to explain the plasmon mode interactions on rather complex nanostructures through hybridization of individual plasmon modes supported by the structure's constitutive elements [45]. In this case, these constitutive elements are the circular disk and the elongated cavity embedded in an infinite uniform gold film. The plasmon hybridization theory models D_1 as a hybrid mode between the dipolar modes of the disk and the cavity. The surface charge distribution on the structure around D_1's resonance frequency (inset of Fig. 2) demonstrates that the dipole moments of these individual dipolar modes are both in the x-direction making D_1 a bonding state hybrid mode. It should be noted here that the anti-boding state hybridized dipole mode cannot be excited with this incident field since the fully asymmetric charge distributions generated by the dipolar modes of the disk and the cavity cancels out the net dipole moment along the x-axis.

2.2. Disk with Shifted Elongated Cavity

To allow for generation of higher order plasmon modes in the visible spectrum under the same excitation, a structural asymmetry is introduced in the initial design [Fig. 1(b)]. The elongated cavity with length $L = 65.5\,\text{nm}$ and width $W = 35\,\text{nm}$ is shifted along the x-axis by $O = 15.25\,\text{nm}$. This breaks the structural symmetry (with respect to the excitation) of the initial design permitting incident field's energy to couple to the higher order modes. This is clearly indicated by the extinction CS spectrum presented in Fig. 3(a); two distinct plasmon modes are identified: A dipolar mode (named D_2) and a quadrupolar mode (named Q_1).

Like D_1, D_2 is a bonding state hybrid mode between dipolar modes of the circular disk and the shifted elongated cavity embedded in an infinite uniform gold film (Section 2.1). This is clearly demonstrated by the charge distribution on the structure around D_2's resonance frequency (inset of Fig. 3(a), frequency marked with the blue dot). The mode Q_1, which remains dark in the initial design, is a hybrid mode between the quadrupolar modes of the disk and the cavity. This is clearly shown by the charge distribution on the structure around Q_1's resonance frequency (inset of Fig. 3(a), frequency marked with the green dot); the charge is distributed in the form of hybrid quadrupolar modes (one around the outer surface of the disk and another on the inner surface of the cavity). It should also be noted here that Q_1 is made dipole active through symmetry breaking; its charge distribution has a non-zero net dipole moment along the x-axis. This clearly explains why the x-polarized incident field excites Q_1.

The asymmetric/non-concentric configuration of the circular disk

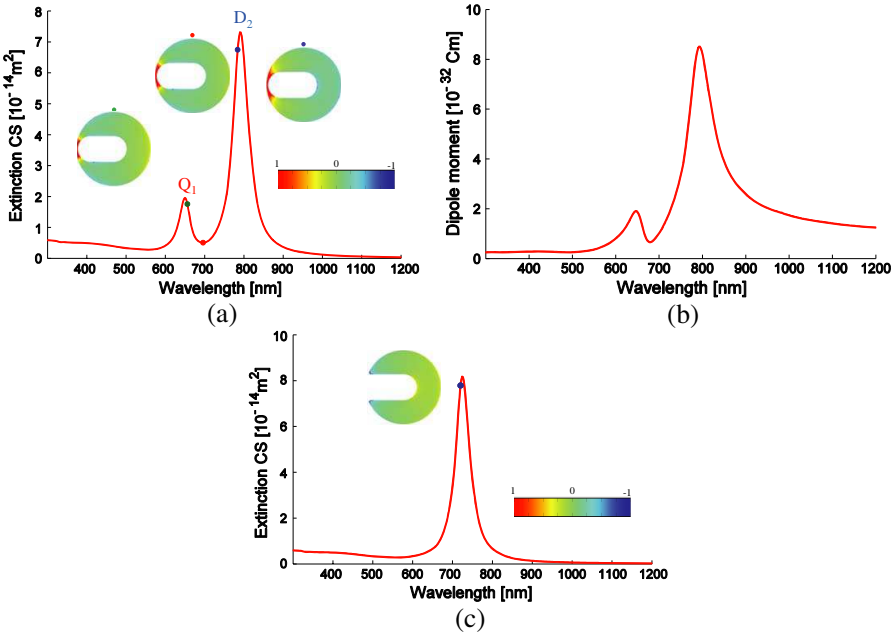

Figure 3. (a) Extinction CS spectrum of the circular disk with the shifted elongated cavity. The geometry parameters shown in Fig. 1(b) and the height of the structure are $D = 100\,\text{nm}$, $L = 65.5\,\text{nm}$, $W = 35\,\text{nm}$, $O = 15.25\,\text{nm}$, and $H = 10\,\text{nm}$ respectively. The insets show the charge distributions on the structure at 656 nm (marked with the green dot on the plot), 696 nm (marked with the red dot), and 784 nm (marked with the blue dot). (b) Amplitude of the net dipole moment along the x-axis. (c) Extinction spectrum of the structure without the "wire". The inset shows the charge distribution on the structure at 720 nm (marked with the blue dot on the plot).

and the elongated cavity creates a thin "wire" on the narrower side between the disk and the cavity. The plasmon modes' electric field amplitudes reach to the maximum around the thinnest section of the wire indicating that the coupling between the modes is strongest along the thinnest section [46]. As a result, one can argue that the thickness of the wire determines the strength of plasmon coupling between modes of the disk and the cavity. Thinner wire means stronger hybridization and larger energy split between the bonding and anti-bonding states. It should be noted here that completely removing the wire (which results in a horseshoe shaped structure) eliminates Q_1. This is clearly shown by the extinction CS spectrum of the horseshoe shaped structure

presented in Fig. 3(c). Obviously, even an asymmetric configuration for this shape fails to generate a higher order mode in the visible spectrum.

Extinction CS spectrum of the circular disk with the shifted elongated cavity [Fig. 3(a)] shows that D_2 and Q_1 overlap spectrally. As expected the super-radiant D_2 is wider while the sub-radiant Q_1 is narrower. The destructive interference between these two modes generates a Fano resonance dip. The charge distribution around the dip (inset of Fig. 3(a), frequency marked with the red dot) reveals that the net dipole moment along the x-axis is cancelled due to overlapping of the modes D_2 and Q_1. This explains why the x-polarized incident field's energy does not couple to the structure around the Fano resonance. The difference in the modes' extinction CS amplitudes can be explained by the difference in the amount of energy they can receive from the incident field. The amount of energy coupled to a mode is related to the amplitude of that mode's net dipole moment along the incident field's polarization. This is demonstrated by Fig. 3(b), where the amplitude of the net dipole moment along the x-axis is provided; as expected, the locations of the peaks of the dipole moment and their relative amplitudes match to those of the extinction CS. Additionally, this figure clearly demonstrates the destructive cancellation of the dipole moment along the x-axis around the Fano resonance.

Next, the effect of filling the shifted elongated cavity on the resonance frequencies of D_2 and Q_1 is characterized. The cavity is filled with silica (refractive index $n = 1.5$) and as expected due to change in the optical path length of the resonance and demonstrated by the extinction CS spectrum provided in Fig. 4(a), resonances of D_2 and Q_1 red shift [47]. Additionally, Fig. 4(a) reveals that the change in the amplitude of the extinction CS of Q_1 is significantly higher than that of D_2. When the cavity is filled with silica, the effective optical size of its inner surface increases. This provides effectively a larger area for charges to distribute. Since Q_1's charge distribution has more variations (when compared to that of D_2, where only one positive and one negative peak exist), its dipole moment is more sensitive to the optical size of the inner surface. Therefore, as expected, the the amplitude of Q_1's extinction CS is more sensitive to the refractive index of the material filling in the cavity. This also suggests that the electrical size of the cavity can be used to tune the Fano resonance. To further demonstrate this, cavity's width is changed from $W = 20\,\text{nm}$ to $W = 45\,\text{nm}$ with a step of $5\,\text{nm}$. Fig. 4(b) plots the extinction CS spectrum for each value of W; the resonances of the D_2 and Q_1 red shift as the width of the cavity increases. Additionally, the figure reveals that the overlap between D_2 and Q_1 increases as the width of the cavity decreases (since the spectral shift in the resonance of D_2 is

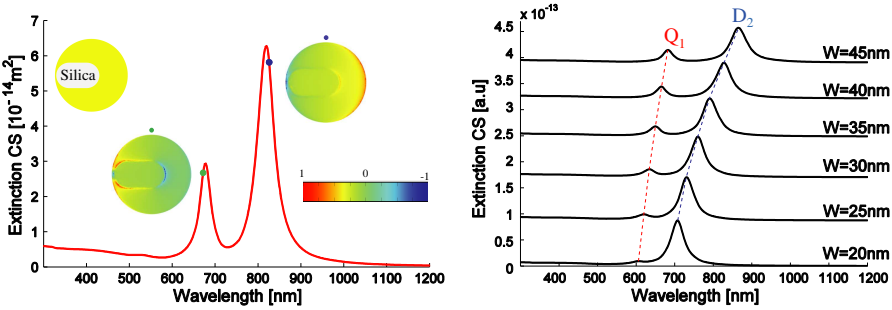

Figure 4. Tunability of the design with the circular disk and the shifted elongated cavity. (a) Extinction CS spectrum of the design with the cavity filled with silica (refractive index $n = 1.5$). (b) Extinction CS spectra of the designs where the cavity's width is changed from $W = 20\,\text{nm}$ to $W = 45\,\text{nm}$ with a step of $5\,\text{nm}$ while the other parameters are $D = 100\,\text{nm}$, $L = 65.5\,\text{nm}$, $O = 15.25\,\text{nm}$, and $H = 10\,\text{nm}$.

larger than that of Q_1). Consequently, the asymmetric line shape of the Fano resonance improves with the decreasing cavity size (i.e., fill factor).

2.3. Disk with Shifted and Rotated Elongated Cavity

Rotating the shifted elongated cavity around the normal of the disk introduces an additional structural asymmetry to the design [Fig. 1(c)]. Here, θ is the angle that the elongated cavity's major axis makes with the x-axis at its center. Consider, for example, the design with $\theta = 40^{\text{o}}$; an x-polarized plane wave normally incident on this structure generates three plasmon modes as demonstrated by the extinction CS spectrum provided in Fig. 5(a). Two of these modes are dipolar modes (named D_3 and D_4) and one of them is a quadrupolar mode (named Q_2).

As with the previously described modes, the plasmon hybridization theory can be used to describe the physical properties of D_3, D_4, and Q_2. Like D_1 (Section 2.1) and D_2 (Section 2.2), D_3 and D_4 are hybrid modes between the dipolar modes of the circular disk and the shifted and rotated elongated cavity embedded in an infinite uniform gold film. This is clearly demonstrated by the charge distributions on the structure around the resonance frequencies of D_3 and D_4 (inset of Fig. 5(a), frequencies marked with the blue and black dots, respectively). Dipole of moment of D_3's charge distribution is largest along the major axis of the cavity but still has a non-zero value along the x-

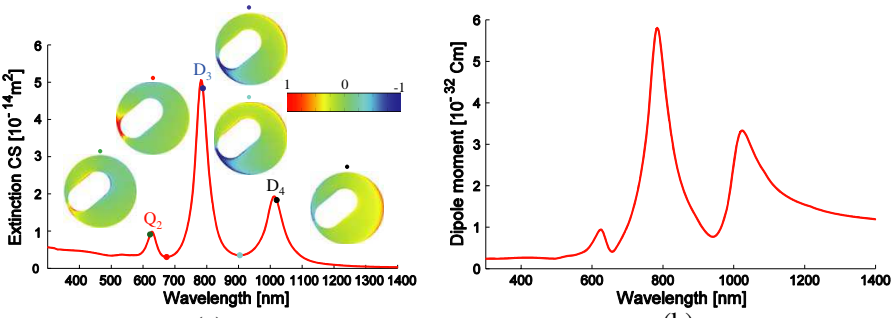

Figure 5. (a) Extinction CS spectrum of the circular disk with the shifted and rotated elongated cavity. The geometry parameters shown in Fig. 1(c) and the height of the structure are $D = 100\,\text{nm}$, $L = 65.5\,\text{nm}$, $W = 35\,\text{nm}$, $O = 15.25\,\text{nm}$, $\theta = 40^{\text{o}}$, and $H = 10\,\text{nm}$, respectively. The insets show the charge distribution on the structure at 622 nm (marked with the green dot on the plot), 674 nm (marked with the red dot), 788 nm (marked with the blue dot), 904 nm (marked with the cyan dot), and 1020 nm (marked with the black dot). (b) Amplitude of the net dipole moment along the x-axis.

axis and the dipole moment of D_4's charge distribution is largest along the x-axis. Like Q_1 (Section 2.2), Q_2 is a hybrid mode between the quadrupolar modes of the disk and the cavity. Charge distribution on the structure around Q_2's resonance frequency (inset of Fig. 5(a), frequency marked with the green dot) shows that Q_2 also has a non-zero dipole moment along the x-axis. Presence of non-zero dipole moments along the x-axis for D_3, D_4, and Q_2 explains why the x-polarized incident field excites these modes.

As clearly shown in Fig. 5(a), the super-radiant mode D_3 spectrally overlaps with both D_4 and Q_2. The super-radiant D_3 is wider while the sub-radiant D_4 and Q_2 are narrower. The destructive interference between Q_2 and D_3 and D_3 and D_4 generate two Fano resonance dips in the visible spectrum. The presence of destructive interference between Q_2 and D_3 and D_3 and D_4 is demonstrated by the charge distributions around the Fano resonance dips (the inset of Fig. 5(a), frequencies marked with the red and cyan dots). Around the Fano resonance frequencies, the net dipole moment along the x-axis is cancelled due to spectral overlapping of the modes, which generate dipole moments in opposite directions. This explains why the x-polarized incident fields energy does not couple to the structure around the Fano resonances.

As discussed in Section 2.2, the extinction CS amplitude of a

mode depends on the energy it can receive from the incident field and hence the net dipole moment along the field's polarization. This is demonstrated by Fig. 5(b), where the amplitude of the net dipole moment along the x-direction is provided; as expected, the locations of the peaks of the dipole moment and their relative amplitudes match to those of the extinction CS.

Next, the effect of the rotation angle θ [measured from the x-axis, Fig. 1(c)] of the shifted elongated cavity on the resonance frequencies of D_3, D_4, and Q_2 is characterized: θ is changed from 10° to 90° with a step of 20°; the extinction CS spectrum computed for each value of θ is provided in Fig. 6. As demonstrated by the figure, the extinction CS amplitude peak that corresponds to D_4 gets intensified while those that correspond to D_3 and Q_2 turn off as θ changes from 10° to 90°. As discussed before, this can be explained by the change in the mode's net dipole moment along the x-axis as θ changes. For example, for $\theta = 90°$, D_3's dipole moment along x-axis vanishes, and the mode cannot be excited with an x-polarized incident field any more. As a result the extinction CS amplitude of D_3 vanishes.

3. RLC CIRCUIT MODEL

The optical response of the shifted (and rotated) elongated cavity can be replicated using an electrical oscillator that can support multiple resonances. In this work, the RLC circuit shown in Fig. 7(a) is used for this purpose; the mathematical model of this RLC circuit is similar

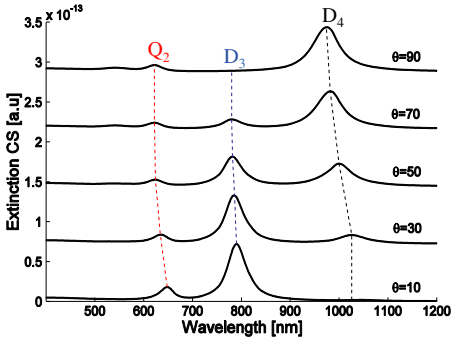

Figure 6. Tunability of the design with the circular disk and the shifted and rotated elongated cavity. Extinction spectra of the designs where the cavity's rotation angle is changed 10° to 90° with a step of 20° while the other parameters are $D = 100\,\text{nm}$, $L = 65.5\,\text{nm}$, $O = 15.25\,\text{nm}$, and $H = 10\,\text{nm}$.

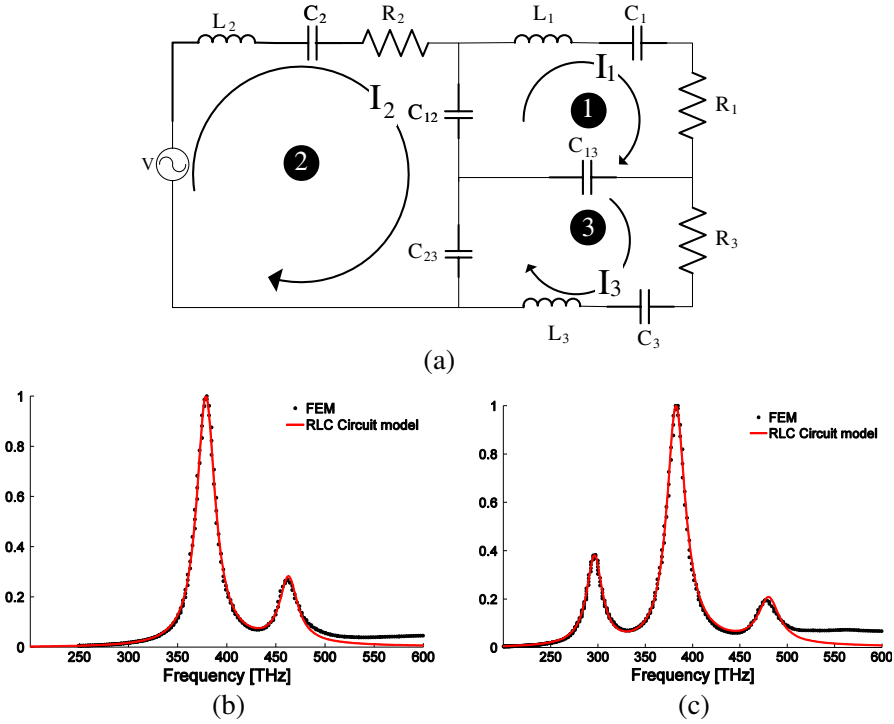

Figure 7. (a) Description of the RLC circuit that supports three resonances. (b) Normalized spectra of P for the circuit with $\gamma_1 = 21.76\,\text{THz}$, $\gamma_2 = 23.03\,\text{THz}$, $\omega_1 = 446.98\,\text{THz}$, $\omega_2 = 397.19\,\text{THz}$, $\Omega_{12} = 168.50\,\text{THz}$, and $\Omega_{13} = \Omega_{23} = 0$, and the extinction CS for the design with $D = 100\,\text{nm}$, $W = 35\,\text{nm}$, $L = 65.5\,\text{nm}$, $O = 15.25\,\text{nm}$, and $H = 10\,\text{nm}$. (c) Normalized spectra of P for the circuit with $\gamma_1 = 27.32\,\text{THz}$, $\gamma_2 = 25.52\,\text{THz}$, $\gamma_3 = 18.23\,\text{THz}$, $\omega_1 = 464.29\,\text{THz}$, $\omega_2 = 382.14\,\text{THz}$, $\omega_3 = 321.49\,\text{THz}$, $\Omega_{12} = 188.34\,\text{THz}$, $\Omega_{13} = 125.77\,\text{THz}$, and $\Omega_{23} = 145.20$, and the extinction CS for the design with $D = 100\,\text{nm}$, $W = 35\,\text{nm}$, $L = 65.5\,\text{nm}$, $O = 15.25\,\text{nm}$, $H = 10\,\text{nm}$, and $\theta = 40^{\text{o}}$.

to that of the mass-spring oscillator developed in [53] to model two distinct Fano resonances. The spectrum of the power drawn by the RLC circuit can be used to mathematically imitate the extinction CS spectrum of the designs with two plasmon modes D_2 and Q_1 (Section 2.2) and three plasmon modes D_3, D_4, and Q_2 (Section 2.3). The circuit consists of three loops of resistive, inductive, and capacitive elements (R_i, L_i, and C_i, $i = 1, 2, 3$), which are coupled using

capacitive elements (C_{12}, C_{13}, and C_{23}). Each loop corresponds to one plasmon mode: Combination of inductive and capacitive elements in each loop generates a resonance while the resistive element accounts for the energy dissipation (due to radiation and ohmic loss). The electromagnetic field incident on the designs is modeled as a time harmonic voltage source, $V_s(t) = \mathrm{Re}\{Ve^{j\omega t}\}$, feeding the loop 2, which represents the dipolar mode that is excited by the incident field. Applying Kirchhoff voltage law to each of the loops in the direction of the arrows as shown in Fig. 7(a) yields a coupled system of equations

$$\begin{aligned}
&\left[-\omega^2 L_1 + j\omega R_1 + \frac{1}{C_1} + \frac{1}{C_{12}} + \frac{1}{C_{13}}\right] I_1 - \frac{I_2}{C_{12}} - \frac{I_3}{C_{13}} = 0 \\
&\left[-\omega^2 L_2 + j\omega R_2 + \frac{1}{C_2} + \frac{1}{C_{12}} + \frac{1}{C_{23}}\right] I_2 - \frac{I_1}{C_{12}} - \frac{I_3}{C_{23}} = V \\
&\left[-\omega^2 L_3 + j\omega R_3 + \frac{1}{C_3} + \frac{1}{C_{13}} + \frac{1}{C_{23}}\right] I_3 - \frac{I_1}{C_{13}} - \frac{I_2}{C_{23}} = 0
\end{aligned} \tag{1}$$

where I_i represents the current on loop i, $i = 1, 2, 3$. Expressing I_i as the rate of change of charge, i.e., $I_i = j\omega q_i$, in the coupled system of Equation (1), one can obtain:

$$\begin{aligned}
&\Gamma_1 q_1 - \Omega_{12}^2 q_2 - \Omega_{13}^2 q_3 = 0 \\
&\Gamma_2 q_2 - \Omega_{12}^2 q_1 - \Omega_{23}^2 q_3 = V/L_2 \\
&\Gamma_3 q_3 - \Omega_{13}^2 q_1 - \Omega_{23}^2 q_2 = 0
\end{aligned} \tag{2}$$

where $\Gamma_i = -\omega^2 + j\omega\gamma_i + \omega_i^2$, $\omega_i = 1/(L_i C_{eqi})^{0.5}$ is the natural resonance frequency of the loop i, $\gamma_i = R_i/L_i$ and C_{eqi} represent its damping coefficient and equivalent capacitance (assuming other loops are open), respectively, and $\Omega_{ij} = 1/(L_i C_{ij})^{0.5}$ is the coupling coefficient between the loops i and j. Here, C_{eqi}, $i = 1, 2, 3$, are given by $1/C_{eq1} = 1/C_1 + 1/C_{12} + 1/C_{13}$, $1/C_{eq2} = 1/C_2 + 1/C_{12} + 1/C_{23}$, and $1/C_{eq3} = 1/C_3 + 1/C_{13} + 1/C_{13}$.

Given the phasor of the voltage source, V, to obtain an expression for the time average total power drawn by the circuit, P, one should known I_2. Coupled system of Equation (2) can be solved for q_2; then an expression for I_2 can be obtained using $I_2 = j\omega q_2$. Inserting this in $P = 0.5\mathrm{Re}\{VI_2^*\}$ yields an expression for P:

$$\begin{aligned}
P \;=\; 0.5|V|^2 \mathrm{Re}\Big\{ & j\omega \left(\Omega_{13}^4 - \Gamma_1\Gamma_3\right) / \Big(L_2 \left[2\Omega_{12}^2\Omega_{13}^2\Omega_{23}^2 \right. \\
& \left. + \Omega_{23}^4\Gamma_1 + \Omega_{12}^4\Gamma_3 + \Gamma_2\left(\Omega_{13}^4 - \Gamma_1\Gamma_3\right)\right]\Big)\Big\}
\end{aligned} \tag{3}$$

As mentioned above, P can be used to mathematically imitate the extinction CS of the designs supporting D_2 and Q_1 and D_3, D_4, and Q_2. The P vs. ω curve described by Equation (3) is numerically fitted to the extinction CS spectra, which are obtained via the finite element simulations, using the Levenberg-Marquardt algorithm implemented within OriginLab commercial software [54]. The algorithm produces the parameters Ω_{12}, Ω_{13}, Ω_{23}, γ_i, and ω_i, $i = 1, 2, 3$, which can then be used to find R_i, L_i, and C_i, $i = 1, 2, 3$. First, the design that supports D_2 and Q_1 is considered. For this case, $\Omega_{13} = \Omega_{23} = 0$, since loops 2 and 1 model D_2 and Q_1, respectively, while loop 3 is left unpowered, i.e., short-circuited. As shown in Fig. 7(b), choosing $\gamma_1 = 21.76\,\text{THz}$, $\gamma_2 = 23.03\,\text{THz}$, $\omega_1 = 446.98\,\text{THz}$, $\omega_2 = 397.19\,\text{THz}$, and $\Omega_{12} = 168.50\,\text{THz}$, normalized spectrum of P is matched to that of the extinction CS for the design with $D = 100\,\text{nm}$, $W = 35\,\text{nm}$, $L = 65.5\,\text{nm}$, $O = 15.25\,\text{nm}$, and $H = 10\,\text{nm}$. Next, the design that supports D_3, D_4, and Q_2 is considered. For this case, loops 1, 2, and 3 are all active and they model D_3, D_4, and Q_2, respectively. As shown in Fig. 7(c), choosing $\gamma_1 = 27.32\,\text{THz}$, $\gamma_2 = 25.52\,\text{THz}$, $\gamma_3 = 18.23\,\text{THz}$, $\omega_1 = 464.29\,\text{THz}$, $\omega_2 = 382.14\,\text{THz}$, $\omega_3 = 321.49\,\text{THz}$, $\Omega_{12} = 188.34\,\text{THz}$, $\Omega_{13} = 125.77\,\text{THz}$, and $\Omega_{23} = 145.20\,\text{THz}$, normalized spectrum of P is matched to that of the extinction CS for the design with $D = 100\,\text{nm}$, $W = 35\,\text{nm}$, $L = 65.5\,\text{nm}$, $O = 15.25\,\text{nm}$, $H = 10\,\text{nm}$, and $\theta = 40°$.

4. SIMULATION PARAMETERS

The electromagnetic wave interactions on the plasmonic nanostructure design proposed in this paper cannot be computed using (semi-) analytical methods. To this end, all field interaction computations are carried out using the RF module of the commercially available Finite Element based software package COMSOL Multiphysics 3.5a [48]. The computation domain is truncated using a 50 nm thick perfectly matched layer (PML) introduced on a spherical surface with radius 250 nm (measured from the center of the disk). On the outer surface of the PML, scattering boundary conditions are enforced. The scattered field formulation is used to introduce the normally incident x-polarized plane wave into the computation domain.

The empirically determined dispersive and complex refractive index of the bulk gold, which is known as Johnson and Christy model [49], is used in all COMSOL simulations. A table listing values of the complex dielectric constant measured at frequency samples are provided in [50]; linear interpolation is used to compute dielectric constant values at frequencies in between these samples.

The absorption CS is calculated by integrating the time average resistive heating in the volume of the gold disk [7]. The scattering CS is calculated by integrating the time average radiated field power density on a spherical surface, which encloses the structure, in the far-field region. The extinction CS is obtained by summing the absorption and scattering CSs.

The charges induced on the surface of the structure are computed from the boundary conditions on the normal component of the electric field. The charges induced in the volume of the structure are computed from the divergence of the electric field. In dipole moment computations, both surface and volume charges are taken into account.

5. CONCLUSION

The presence of Fano resonances in the optical response of a sub-wavelength planar metallic nanostructure to normally incident and linearly polarized electromagnetic field is demonstrated. The nanostructure is constructed from a circular gold disk embedding an elongated cavity. The symmetry of the structure with respect to the incident field is broken by shifting and rotating the elongated cavity. The spectral overlaps between the super-radiant plasmon mode and the sub-radiant ones, which are induced due to symmetry breaking, result in two distinct Fano resonances in the visible spectrum. It is shown that these resonances can be tuned by varying the geometry parameters, especially the width and the rotation angle of the elongated cavity. Additionally, extinction CS of the proposed design is compared to the total power drawn by an RLC circuit, representing a mathematical model analogue to a mass-spring oscillator.

Results presented in this work suggest that arrays constructed from various combinations of the proposed design can be used in several interesting applications, where the presence of two distinct Fano resonance regions can be particularly useful. One interesting example of such applications is bio- and chemical particle detection using slow light. Detailed theoretical and numerical analysis of such arrays and their applications will be carried out in a future work.

ACKNOWLEDGMENT

This work was supported in part by a Academic Excellence Alliance (AEA) program award from King Abdullah University of Science and Technology (KAUST) Global Collaborative Research (GCR) under the title "Energy Efficient Photonic and Spintronic Devices".

REFERENCES

1. Halas, N. J., S. Lal, W.-S. Chang, S. Link, and P. Nordlander, "Plasmons in strongly coupled metallic nanostructures," *Chem. Rev.*, Vol. 111, No. 6, 3913–3961, 2011.
2. Mortazavi, D., A. Z. Kouzani, A. Kaynak, and W. Duan, "Developing LSPR design guidelines," *Progress In Electromagnetics Research*, Vol. 126, 203–235, 2012.
3. Lal, S., S. Link, and N. J. Halas, "Nano-optics from sensing to waveguiding," *Nat. Photonics*, Vol. 1, No. 11, 641–648, 2007.
4. Brandl, D. W., N. A. Mirin, and P. Nordlander, "Plasmon modes of nanosphere trimers and quadrumers," *J. Phys. Chem. B*, Vol. 110, No. 25, 12302–12310, 2006.
5. Chau, Y.-F., Z.-H. Jiang, H.-Y. Li, G.-M. Lin, F.-L. Wu, and W.-H. Lin, "Localized resonance of composite core-shell nanospheres, nanobars and nanospherical chains," *Progress In Electromagnetics Research B*, Vol. 28, 183–199, 2011.
6. Renger, J., S. Grafström, L. Eng, and V. Deckert, "Evanescent wave scattering and local electric field enhancement at ellipsoidal silver particles in the vicinity of a glass surface," *J. Opt. Soc. Am. A*, Vol. 21, No. 7, 1362–1367, 2004.
7. Mark, W. K. and J. H. Naomi, "Nanoshells to nanoeggs to nanocups: Optical properties of reduced symmetry coreshell nanoparticles beyond the quasistatic limit," *New J. Phys.*, Vol. 10, No. 10, 105006, 2008.
8. Hu, Y., S. Noelck, and R. Drezek, "Symmetry breaking in gold-silica-gold multilayer nanoshells," *ACS Nano*, Vol. 4, No. 3, 1521–1528, 2010.
9. Hao, F., P. Nordlander, Y. Sonnefraud, P. Dorpe, and S. Maier, "Tunability of subradiant dipolar and Fano-type plasmon resonances in metallic ring/disk cavities: Implications for nanoscale optical sensing," *ACS Nano*, Vol. 3, No. 3, 643–652, 2009.
10. Aizpurua, J., P. Hanarp, D. S. Sutherland, M. Käll, G. W. Bryant, and F. J. Garcia De Abajo, "Optical properties of gold nanorings," *Phys. Rev. Lett.*, Vol. 90, No. 5, 057401, 2003.
11. Ishimaru, A., S. Jaruwatanadilok, and Y. Kuga, "Generalized surface plasmon resonance sensors using metamaterials and negative index materials," *Progress In Electromagnetics Research*, Vol. 51, 139–152, 2005.
12. Raymond Ooi, C. H., "Near-field and particle size effects in coherent raman scattering," *Progress In Electromagnetics*

Research, Vol. 117, 479–494, 2011.

13. Liu, X., J. Lin, T. F. Jiang, Z. F. Zhu, Q. Q. Zhan, J. Qian, and S. He, "Surface plasmon properties of hollow AuAg alloyed triangular nanoboxes and its applications in SERS imaging and potential drug delivery," *Progress In Electromagnetics Research*, Vol. 128, 35–53, 2012.
14. Luo, Z., T. Suyama, X. Xu, and Y. Okuno, "A grating-based plasmon biosensor with high resolution," *Progress In Electromagnetics Research*, Vol. 118, 527–539, 2011.
15. Gong, Y., K. Li, J. Huang, N. J. Copner, A. Davies, L. Wang, and T. Duan, "Frequency-selective nanostructured plasmonic absorber by highly lossy interface mode," *Progress In Electromagnetics Research*, Vol. 124, 511–525, 2012.
16. Li, M., H.-L. Yang, X.-W. Hou, Y. Tian, and D.-Y. Hou, "Perfect metamaterial absorber with dual bands," *Progress In Electromagnetics Research*, Vol. 108, 37–49, 2010.
17. Han, L., S. Chen, A. Schulzgen, Y. Zeng, F. Song, J.-G. Tian, and N. Peyghambarian, "Calculation and optimization of electromagnetic resonances and local intensity enhancements for plasmon metamaterials with sub-wavelength double-slots," *Progress In Electromagnetics Research*, Vol. 113, 161–177, 2011.
18. Rahimi, H., A. Namdar, S. Roshan Entezar, and H. Tajalli, "Photonic transmission spectra in one-dimensional fibonacci multilayer structures containing single-negative metamaterials," *Progress In Electromagnetics Research*, Vol. 102, 15–30, 2010.
19. Li, J., F.-Q. Yang, and J. Dong, "Design and simulation of l-shaped chiral negative refractive index structure," *Progress In Electromagnetics Research*, Vol. 116, 395–408, 2011.
20. Carbonell, J., E. Lheurette, and D. Lippens, "From rejection to transmission with stacked arrays of split ring resonators," *Progress In Electromagnetics Research*, Vol. 112, 215–224, 2011.
21. Zhang, J. and N. A. Mortensen, "Ultrathin cylindrical cloak," *Progress In Electromagnetics Research,* Vol. 121, 381–389, 2011.
22. Larsson, E. M., J. Alegret, M. Käll, and D. S. Sutherland, "Sensing characteristics of NIR localized surface plasmon resonances in gold nanorings for application as ultrasensitive biosensors," *Nano Lett.*, Vol. 7, No. 5, 1256–1263, 2007.
23. Miroshnichenko, A. E., S. Flach, and Y. S. Kivshar, "Fano resonances in nanoscale structures," *Rev. Mod. Phys.*, Vol. 82, No. 3, 2257–2298, 2010.
24. Abbasian, K., A. Rostami, and Z. D. Koozehkanani, "All-

optical tunable mirror design using electromagnetically induced transparency," *Progress In Electromagnetics Research M*, Vol. 5, 25–41, 2008.

25. Liu, Y., H. Jiang, C. Xue, W. Tan, H. Chen, and Y. Shi, "Fano resonances in a bilayer structure composed of two kinds of dispersive metamaterials," *Progress In Electromagnetics Research Letters*, Vol. 26, 49–57, 2011.
26. Luk'yanchuk, B., N. Zheludev, S. Maier, N. Halas, P. Nordlander, H. Giessen, and C. Chong, "The Fano resonance in plasmonic nanostructures and metamaterials," *Nat. Mater.*, Vol. 9, No. 9, 707–715, 2010.
27. Papasimakis, N. and N. I. Zheludev, "Metamaterial-induced transparency: Sharp Fano resonances and slow light," *Opt. Photonics News*, Vol. 20, No. 10, 22–27, 2009.
28. Bao, K., N. Mirin, and P. Nordlander, "Fano resonances in planar silver nanosphere clusters," *Appl. Phys. A*, Vol. 100, No. 2, 333–339, 2010.
29. Fan, J., C. Wu, K. Bao, J. Bao, R. Bardhan, N. Halas, V. Manoharan, P. Nordlander, G. Shvets, and F. Capasso, "Self-assembled plasmonic nanoparticle clusters," *Science*, Vol. 328, No. 5982, 1135, 2010.
30. Liu, S.-D., Z. Yang, R.-P. Liu, and X.-Y. Li, "Plasmonic-induced optical transparency in the near-infrared and visible range with double split nanoring cavity," *Opt. Express*, Vol. 19, No. 16, 15363–15370, 2011.
31. Yang, Z.-J., Z.-S. Zhang, L.-H. Zhang, Q.-Q. Li, Z.-H. Hao, and Q.-Q. Wang, "Fano resonances in dipole-quadrupole plasmon coupling nanorod dimers," *Opt. Lett.*, Vol. 36, No. 9, 1542–1544, 2011.
32. Fan, J. A., K. Bao, C. Wu, J. Bao, R. Bardhan, N. J. Halas, V. N. Manoharan, G. Shvets, P. Nordlander, and F. Capasso, "Fano-like interference in self-assembled plasmonic quadrumer clusters," *Nano Lett.*, Vol. 10, No. 11, 4680–4685, 2010.
33. Verellen, N., Y. Sonnefraud, H. Sobhani, F. Hao, V. V. Moshchalkov, P. V. Dorpe, P. Nordlander, and S. A. Maier, "Fano resonances in individual coherent plasmonic nanocavities," *Nano Lett.*, Vol. 9, No. 4, 1663–1667, 2009.
34. Liu, H., N. Wang, Y. Liu, Y. Zhao, and X. Wu, "Light transmission properties of double-overlapped annular apertures," *Opt. Lett.*, Vol. 36, No. 3, 385–387, 2011.
35. Mukherjee, S., H. Sobhani, J. B. Lassiter, R. Bardhan,

P. Nordlander, and N. J. Halas, "Fanoshells: Nanoparticles with built-in Fano resonances," *Nano Lett.*, Vol. 10, No. 7, 2694–2701, 2010.

36. Sonnefraud, Y., N. Verellen, H. Sobhani, G. A. E. Vandenbosch, V. V. Moshchalkov, P. Van Dorpe, P. Nordlander, and S. A. Maier, "Experimental realization of subradiant, superradiant, and Fano resonances in ring/disk plasmonic nanocavities," *ACS Nano*, Vol. 4, No. 3, 1664–1670, 2010.
37. Singh, R., I. A. I. Al-Naib, M. Koch, and W. Zhang, "Sharp Fano resonances in THz metamaterials," *Opt. Express*, Vol. 19, No. 7, 6312–6319, 2011.
38. Dong, Z.-G., H. Liu, M.-X. Xu, T. Li, S.-M. Wang, J.-X. Cao, S.-N. Zhu, and X. Zhang, "Role of asymmetric environment on the dark mode excitation in metamaterial analogue of electromagnetically-induced transparency," *Opt. Express*, Vol. 18, No. 21, 22412–22417, 2010.
39. Ourir, A., R. Abdeddaim, and J. de Rosny, "Tunable trapped mode in symmetric resonator designed for metamaterials," *Progress In Electromagnetics Research*, Vol. 101, 115–123, 2010.
40. Habteyes, T. G., S. Dhuey, S. Cabrini, P. J. Schuck, and S. R. Leone, "Theta-shaped plasmonic nanostructures: Bringing 'dark' multipole plasmon resonances into action via conductive coupling," *Nano Lett.*, Vol. 11, No. 4, 1819–1825, 2011.
41. Fang, Z., J. Cai, Z. Yan, P. Nordlander, N. J. Halas, and X. Zhu, "Removing a wedge from a metallic nanodisk reveals a Fano resonance," *Nano Lett.*, Vol. 11, No. 10, 4475–4479, 2011.
42. Rahmani, M., B. Luk'yanchuk, B. Ng, A. K. G. Tavakkoli, Y. F. Liew, and M. H. Hong, "Generation of pronounced Fano resonances and tuning of subwavelength spatial light distribution in plasmonic pentamers," *Opt. Express*, Vol. 19, No. 6, 4949–4956, 2011.
43. Rahmani, M., T. Tahmasebi, Y. Lin, B. Luk'yanchuk, T. Liew, and M. Hong, "Influence of plasmon destructive interferences on optical properties of gold planar quadrumers," *Nanotechnology*, Vol. 22, 245204, 2011.
44. Liu, N., L. Langguth, T. Weiss, J. Kastel, M. Fleischhauer, T. Pfau, and H. Giessen, "Plasmonic analogue of electromagnetically induced transparency at the drude damping limit," *Nat. Mater.*, Vol. 8, No. 9, 758–762, 2009.
45. Prodan, E., C. Radloff, N. J. Halas, and P. Nordlander, "A hybridization model for the plasmon response of complex nanostructures," *Science*, Vol. 302, No. 5644, 419–422, 2003.

46. Wang, H., Y. Wu, B. Lassiter, C. Nehl, J. Hafner, P. Nordlander, and N. Halas, "Symmetry breaking in individual plasmonic nanoparticles," *PNAS*, Vol. 103, No. 29, 10856, 2006.
47. Bardhan, R., N. K. Grady, T. Ali, and N. J. Halas, "Metallic nanoshells with semiconductor cores: Optical characteristics modified by core medium properties," *ACS Nano*, Vol. 4, No. 7, 6169–6179, 2010.
48. Multiphysics, C., V. 3.5 a, COMSOL AB, Sweden, 2009.
49. Johnson, P. and R. Christy, "Optical constants of the noble metals," *Phys. Rev. B*, Vol. 6, No. 12, 4370–4379, 1972.
50. Ni, X., Z. Liu, and A. V. Kildishev, "PhotonicsDB: Optical constants," 2008, doi: 10254/nanohub-r3692.10.
51. Park, T.-H., "Plasmonic properties of metallic nanostructures," Ph.D. Thesis, Rice University, Houstan Texas, 2009.
52. Kang, L., V. Sadaune, and D. Lippens, "Numerical analysis of enhanced transmission through a single subwavelength aperture based on Mie resonance single particle," *Progress In Electromagnetics Research*, Vol. 113, 211–226, 2011.
53. Rahmani, M., B. Lukiyanchuk, T. T. V. Nguyen, T. Tahmasebi, Y. Lin, T. Y. F. Liew, and M. H. Hong, "Influence of symmetry breaking in pentamers on Fano resonance and near-field energy localization," *Opt. Mater. Express*, Vol. 1, No. 8, 1409–1415, 2011.
54. http://www.originlab.com, Accessed 5, May 2012.